Journal of Structural Geology 32 (2010) 15–27

Contents lists available at ScienceDirect

Journal of Structural Geology

journal homepage: www.elsevier.com/locate/jsg

Kinematics and dynamics of fault reactivation: The Cosserat approach

Jure Žalohar*, Marko Vrabec

University of Ljubljana, Faculty of Natural Sciences and Engineering, Department of Geology, Aškerčeva 12, SI-1000 Ljubljana, Slovenia

ARTICLE INFO

Article history:
Received 26 December 2008
Received in revised form
10 June 2009
Accepted 11 June 2009
Available online 21 June 2009

Keywords:
Cosserat continuum
Fault reactivation
Fault-slip analysis
Kinematic analysis
Paleostress analysis

ABSTRACT

In the theory of Cosserat continuum, the faulting-related deformation of rocks is described using translational and rotational degrees of freedom, producing definitions for a symmetric macrostrain tensor and a skew-symmetric relative microrotation tensor. The macrostrain tensor describes the large-scale deformation of the region, whilst the relative microrotation tensor describes the difference between the large-scale regional rotation and local systematic microrotations of blocks between faults. Faults are activated when the resolved shear stress in the direction of movement exceeds frictional resistance for sliding, according to Amontons's Law of Friction. The direction of slip along the faults depends on the Cosserat strain tensor, which is defined as the sum of the macrostrain tensor and the relative microrotation tensor. We develop a constitutive relation for the faulting-related strain of rocks (cataclastic flow) based on the *J-2* plasticity model for the Cosserat continuum, from which we derive the generally asymmetric stress tensor. We also develop the Cosserat stress–strain inverse method for fault-slip data analysis. We show that the geometry of fault systems is controlled by both the Cosserat strain tensor and the stress tensor, and present a field example of a fault system that conforms to the predictions of the Cosserat theory.

1. Introduction

Paleostress and kinematic analyses of fault-slip data are generally performed within the frame of the classical continuum theory, where the deformation of a body is described by three degrees of freedom (the components of the translation vector) and where the stresses and the strains are assumed to be symmetrical (e.g. Jaeger and Cook, 1969; Angelier, 1994). Most of the techniques for fault-slip data analysis also suppose that: (1) the stress/strain field at the time of faulting was homogeneous; (2) the faults are independent and do not interact; and (3) the blocks bounded by the faults do not rotate (e.g. Angelier, 1994; Nemcok and Lisle, 1995; Nemcok et al., 1999; Žalohar and Vrabec, 2007). These assumptions are obviously oversimplified and are only acceptable in certain geological situations. In the last two decades considerable progress in understanding the effect of block (micro)rotations between the faults has been made using the Cosserat continuum theory (Twiss et al., 1991, 1993; Twiss and Unruh, 1998; Figueiredo et al., 2004; Twiss and Unruh, 2007). Twiss et al. (1991, 1993), and Twiss and Unruh (1998, 2007) were the first to recognize the influence of block (micro)-rotations on fault-slip patterns. In the Cosserat continuum theory, the direction of slip along the faults depends on the Cosserat strain tensor and not on the stress tensor. From this it follows that the patterns of slip along the faults are related in a systematic way to the global deformation. The (paleo)stress can therefore be reconstructed from fault-slip data provided the rheological behavior of rocks and the constitutive relation between the stress and strain are known. Twiss et al. (1991, 1993) and Twiss and Unruh (1998, 2007) also studied the influence of relative microrotations on the geometry of fault systems. They showed that, in addition to symmetric fault systems with conjugate or orthorhombic geometry predicted by the classical continuum theory, the Cosserat theory also predicts monoclinic and triclinic fault systems.

This article aims to present a fault reactivation model for the Cosserat continuum. We show that strain is not the only parameter affecting the geometry of the slip-capable fault systems. Another controlling parameter is stress, which is not necessarily symmetric. We also develop an improved Cosserat stress–strain inverse method for fault-slip data analysis based on the Cosserat (or micropolar) strain inverse method of Twiss et al. (1991, 1993), and Twiss and Unruh (1998, 2007). Our method is implemented in the T-TECTO 2.0 computer program (available free of charge from: www2.arnes.si/~jzaloh/t-tecto_homepage.htm). The method was thoroughly tested on numerous artificial and natural datasets. We present an analysis of one selected natural fault system, which indicates that in some cases at least, faulted rocks can be successfully described within the frame of the Cosserat theory.

* Corresponding author. Tel.: +386 407 95572.
E-mail address: jure.zalohar@guest.arnes.si (J. Žalohar).

0191-8141/$ – see front matter © 2009 Elsevier Ltd. All rights reserved.
doi:10.1016/j.jsg.2009.06.008

2. Kinematics of the Cosserat continuum

The kinematics of the Cosserat continuum is characterized by a (micro)rotational degree of freedom $\vec{\phi}^{Cosserat}$, which is independent of the translatory motion described by the displacement field $\vec{u}$ (Fig. 1, Table 1). The field of continuum macro-rotations does not coincide with microrotations at each material particle (Iordache and Willam, 1998), and therefore we must consider two scales of deformation: the instantaneous macrodisplacement gradient and the instantaneous microrotation (e.g. Twiss and Unruh, 2007). The former is defined by the relative motions of the centroids of the blocks bounded by the faults, whereas the instantaneous microrotation describes rigid rotation of blocks around their centroids and is independent of the large-scale macrorotation $\vec{\phi}^{macro}$. Therefore, in the Cosserat continuum the corresponding strain measures are the *Cosserat strain tensor* **e** and the *torsion-curvature tensor* **κ** (Forest, 2000; Forest and Sievert, 2003):

$$\mathbf{e} = \mathbf{u} - \mathbf{W}^C = \vec{u} \otimes \vec{\nabla} + \underline{\varepsilon}\, \vec{\phi}^{Cosserat}, \quad \boldsymbol{\kappa} = \vec{\phi}^{Cosserat} \otimes \vec{\nabla}. \qquad (1)$$

Here, $\underline{\varepsilon}$ represents the third-order permutation tensor $\underline{\varepsilon} = \varepsilon_{ijk} = 1/2(i-j)(j-k)(k-i)$, and $\mathbf{W}^C = -\underline{\varepsilon}\, \vec{\phi}^{Cosserat}$ is the *Cosserat microrotation tensor*, which describes the microrotation of the blocks. We have also introduced the *deformation gradient tensor* (or instantaneous macrodisplacement gradient) $\mathbf{u} = u_{ij} = \partial u_j/\partial x_i = \vec{u} \otimes \vec{\nabla}$. The symmetric part $\mathbf{u}^{(S)}$ of this tensor defines the macrostrain, while the skew-symmetric part $\mathbf{u}^{(A)}$ defines the instantaneous macrorotation. Here we use the sign convention from the rock mechanics and paleostress analysis literature, where the strains and stresses are assumed positive for contraction/compression and negative for extension/tension.

The torsion-curvature tensor **κ** takes into account the differential changes of the microrotations in the neighborhood of a point. From the definition of the Cosserat deformation measures (Eq. (1)), it follows that the torsion-curvature tensor and the gradient of Cosserat deformation are related by the equation (Toupin, 1962, 1964; Forest and Sievert, 2003):

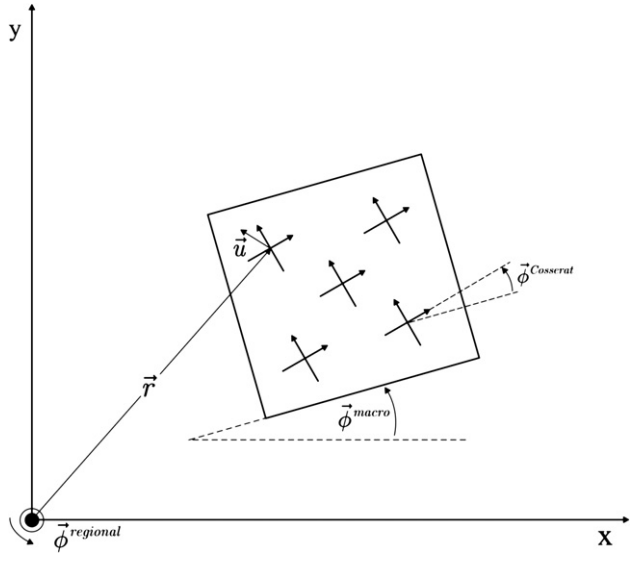

Fig. 1. Micro- and macro-rotations in a Cosserat continuum. $\vec{\phi}^{regional}$ represents the large-scale regional rotation, which is not related to faulting and can be measured by paleomagnetic measurements. $\vec{\phi}^{macro}$ represents the large-scale regional rotation related to faulting (=axial vector of the deformation gradient tensor). $\vec{\phi}^{Cosserat}$ is the Cosserat microrotation of individual segments of the Cosserat continuum. Simplified after Willam and Iordache (2001).

Table 1
Explanation of the most important quantities used in the text.

Symbol	Explanation	First used in Eq.
$\vec{\phi}^{Cosserat}$	Cosserat microrotation vector	(1)
$\vec{\phi}^{macro}$	Regional macrorotation vector	(6)
$\vec{\phi}^{rel}$	Relative microrotation vector	(6)
$\vec{u}$	Translation of material point	(1)
$\vec{\lambda}_1$, $\vec{\lambda}_2$, $\vec{\lambda}_3$	Kinematic axes or eigenvectors of the macrostrain tensor $\mathbf{u}^{(S)}$	(7)
$\lambda_1, \lambda_2, \lambda_3$	Principal strains or eigenvalues of the macrostrain tensor $\mathbf{u}^{(S)}$	(7)
$\vec{n}$	Normal vector to the fault plane	(7)
$\vec{m}$	Slip direction along the fault	(7)
W	Relative microrotation parameter	(10)
L	Distance between the centroids of the neighboring blocks	(13)
$\Omega(\sigma, \mu, R)$	pseudo-potential of dissipation	(19)
$f(\sigma, \mu, R)$	Yield function	(20) and (21)
$\dot{p}$	Rate-of-plastic multiplier	(20) and (24)
q	Material internal variable accounting for material hardening	(20)
R	Thermodynamic force associated with the material internal variables	(19)
J_{2d}	Second invariant of stress and/or couple-stress tensors extended to the Cosserat continuum	(22)
a_1, a_2, b_1, b_2	Material parameters	(22)
p_r, a and b	Parameters in the constitutive equation for the cataclastic flow	(28)
ϕ_1	Maximum possible angle of friction for sliding on pre-existing fault	(39)
ϕ_2	Angle of residual friction	(39)
F_0	Object function in the inverse method	(43)
s, Δ	Parameters related to inhomogeneity of the strain/stress field	(42)
σ_n and τ	Normal and shear stress along the fault	(16)
e	Cosserat strain tensor	(1)
$\mathbf{e}_p$ and $\mathbf{e}_e$	Plastic and elastic parts of the Cosserat strain tensor	(18)
$\mathbf{e}^{(S)}$ and $\mathbf{e}^{(A)}$	Symmetric and skew-symmetric parts of the Cosserat strain tensor	(5) and (26)
κ	Torsion-curvature tensor	(1)
σ	Stress tensor	(15)
$\boldsymbol{\sigma}^d$	Deviatoric part of the stress tensor	(22)
μ	Couple-stress tensor	(15)
$\boldsymbol{\mu}^d$	Deviatoric part of the couple-stress tensor	(22)
$\underline{\varepsilon}$	Third-order permutation tensor	(1)
$\mathbf{W}^C$	Cosserat microrotation tensor	(5)
u	Deformation gradient tensor	(1)
$\mathbf{u}^{(S)}$	Symmetric part of the deformation gradient tensor (=macrostrain tensor)	(3) and (5)
$\mathbf{u}^{(A)}$ and $\mathbf{W}^{macro}$	Skew-symmetric part of the deformation gradient tensor (=macrorotation tensor)	(5)
A	Relative microrotation tensor	(5)
N	Second-order projection tensor	(12)
$\underline{\mathbf{T}}$	Third-order projection tensor	(12)
$\underline{\mathbf{1}}$	Fourth-order identity tensor	(12)

$$\mathbf{e} \otimes \vec{\nabla} = \mathbf{u} \otimes \vec{\nabla} \otimes \vec{\nabla} + \underline{\varepsilon} \cdot \boldsymbol{\kappa}. \qquad (2)$$

By means of the compatibility requirements, the gradient of the mean rotation of the displacement field can be reduced to the gradient of the symmetric part of the displacement gradient:

$$\vec{u} \otimes \vec{\nabla} \otimes \vec{\nabla} = \mathbf{u}^{(S)} \otimes \vec{\nabla} - \underline{\varepsilon} \cdot \underline{\varepsilon} : \left(\vec{\nabla} \otimes \mathbf{u}^{(S)}\right). \qquad (3)$$

As a result, the torsion-curvature tensor is uniquely determined by the gradient of the Cosserat strain tensor (e.g. Toupin, 1962, 1964; Forest and Sievert, 2003):

$$\begin{aligned} \boldsymbol{\kappa} &= \frac{1}{2}\underline{\varepsilon} : \left(\mathbf{e} \otimes \vec{\nabla} + \vec{\nabla} \otimes \left(\mathbf{e} + \mathbf{e}^T\right)\right) \\ &= \frac{1}{2}\varepsilon_{lij}\left(e_{ij,k} + \left(e_{jk} + e_{kj}\right)_i\right). \end{aligned} \qquad (4)$$

This is an important result, since in the description of geological faulting we often take the deformation field to be homogeneous, implying that the gradient of the Cosserat strain tensor is equal to zero. In such a case the torsion-curvature tensor is also equal to zero.

Because the deformation gradient tensor can be decomposed into the symmetric and skew-symmetric parts $\mathbf{u} = \mathbf{u}^{(S)} + \mathbf{u}^{(A)}$, the Cosserat strain tensor can be written as:

$$\mathbf{e} = \mathbf{u}^{(S)} + \mathbf{u}^{(A)} - \mathbf{W}^{C} = \mathbf{u}^{(S)} + \mathbf{A} \tag{5}$$

with $\mathbf{e}^{(S)} = \mathbf{u}^{(S)}$ and $\mathbf{e}^{(A)} = \mathbf{A}$. We have introduced the *relative microrotation tensor*

$$\mathbf{A} = \mathbf{u}^{(A)} - \mathbf{W}^{C} = \mathbf{W}^{macro} - \mathbf{W}^{C} = -\underline{\varepsilon}\left(\vec{\phi}^{macro} - \vec{\phi}^{Cosserat}\right) = -\underline{\varepsilon}\,\vec{\phi}^{rel}. \tag{6}$$

The macrorotation or skew-symmetric part of the displacement gradient tensor is $\mathbf{W}^{macro} = -\underline{\varepsilon}\,\vec{\phi}^{macro}$, with axial vector $\vec{\phi}^{macro}$. The difference $(\vec{\phi}^{macro} - \vec{\phi}^{Cosserat})$ between the macrorotation and microrotation vectors is here termed the *relative microrotation*. Normally, the Cosserat microrotation vector $\vec{\phi}^{Cosserat}$ and macrorotation vector $\vec{\phi}^{macro}$ are axial vectors, which can have any orientation. Following the simplified model of Twiss et al. (1991, 1993) and Twiss and Unruh (1998, 2007), however, we presume that both vectors are parallel to the intermediate eigenvector $\vec{\lambda}_2$ of the macrostrain tensor $\mathbf{u}^{(S)}$, because this is likely to be the most significant component. If $\vec{\lambda}_1, \vec{\lambda}_2, \vec{\lambda}_3$ are the eigenvectors of the macrostrain tensor $\mathbf{u}^{(S)}$, and $\lambda_1, \lambda_2, \lambda_3$ its eigenvalues with $\lambda_1 \geq \lambda_2 \geq \lambda_3$, the deformation gradient tensor owing to slip along a single fault plane with the normal $\vec{n}$ and slip direction $\vec{m}$ can be written in the coordinate system of the eigenvectors $\vec{\lambda}_1, \vec{\lambda}_2$ and $\vec{\lambda}_3$ as:

$$\vec{u} \otimes \vec{\nabla} = \gamma \begin{bmatrix} 1 & 0 & 1 \\ 0 & 0 & 0 \\ -1 & 0 & -1 \end{bmatrix} = \begin{bmatrix} \lambda_1 & 0 & 0 \\ 0 & 0 & 0 \\ 0 & 0 & \lambda_3 \end{bmatrix} + \begin{bmatrix} 0 & 0 & \frac{\lambda_1 - \lambda_3}{2} \\ 0 & 0 & 0 \\ -\frac{\lambda_1 - \lambda_3}{2} & 0 & 0 \end{bmatrix}, \tag{7}$$

where we also choose $\lambda_1 = \gamma$, $\lambda_3 = -\gamma$, $\vec{n} = 1/\sqrt{2}\cdot(\vec{\lambda}_1 + \vec{\lambda}_3)$, $\vec{m} = 1/\sqrt{2}\cdot(-\vec{\lambda}_1 + \vec{\lambda}_3)$, and where γ is the relative amount of contraction and extension in the direction of the $\vec{\lambda}_1$ and $\vec{\lambda}_3$ axes (see Fig. 2). Then the skew-symmetric part or macrorotation tensor is:

$$[\vec{u} \otimes \vec{\nabla}]^{(A)} = \frac{1}{2}\underline{\varepsilon}\,(\vec{u} \times \vec{\nabla}) = -\frac{1}{2}\underline{\varepsilon}\,\vec{\phi}^{macro} = -\frac{1}{2}\underline{\varepsilon}\,(\gamma\vec{\lambda}_2), \tag{8}$$

with axial macrorotation vector $\vec{\phi}^{macro}$ parallel to the intermediate eigenvector of the macrostrain tensor $\vec{\lambda}_2$. Because we also assume the Cosserat microrotation vector $\vec{\phi}^{Cosserat}$ to be parallel to $\vec{\lambda}_2$, it follows that the relative microrotation vector $\vec{\phi}^{rel} = (\vec{\phi}^{macro} - \vec{\phi}^{Cosserat})$ is also parallel to $\vec{\lambda}_2$. The relative microrotation tensor $\mathbf{A}$ can then be written in the coordinate system of the eigenvectors $\vec{\lambda}_1, \vec{\lambda}_2$ and $\vec{\lambda}_3$ as:

$$\mathbf{A} = \begin{pmatrix} 0 & 0 & -W\frac{1}{2}(\lambda_1 - \lambda_3) \\ 0 & 0 & 0 \\ W\frac{1}{2}(\lambda_1 - \lambda_3) & 0 & 0 \end{pmatrix} = \begin{pmatrix} 0 & 0 & \phi^{Cosserat} - \phi^{macro} \\ 0 & 0 & 0 \\ \phi^{macro} - \phi^{Cosserat} & 0 & 0 \end{pmatrix}. \tag{9}$$

Here, we introduce the *relative microrotation (or vorticity) parameter W* (e.g. Twiss and Unruh, 1998, 2007):

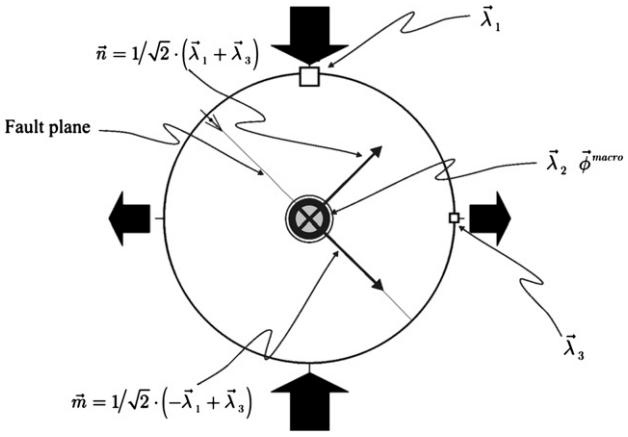

Fig. 2. Orientation of principal strain axes $\vec{\lambda}_1, \vec{\lambda}_2, \vec{\lambda}_3$ of the macrostrain tensor and the macrorotation vector $\vec{\phi}^{macro}$ for the case of a single fault (or fault set) with normal vector $\vec{n}$ and direction of slip $\vec{m}$.

$$W = \frac{\phi^{macro} - \phi^{Cosserat}}{0,5(\lambda_1 - \lambda_3)}. \tag{10}$$

This parameter represents an extra degree of kinematic freedom that describes a normalized measure of the difference between the Cosserat microrotation of the rigid blocks $\vec{\phi}^{Cosserat}$ and the average macrorotation $\vec{\phi}^{macro}$ of the global material lines in the global deformation of the rock continuum (Twiss and Unruh, 1998). The denominator in Eq. (10) is the maximum possible shear strain obtainable from the global macrostrain tensor.

3. The slip direction along the faults

The strain and curvature vectors on each microplane (fault) are given by:

$$\vec{t_e} = \mathbf{e}\vec{n} \quad \text{and} \quad \vec{t_k} = \boldsymbol{\kappa}\vec{n}. \tag{11}$$

We are particularly interested in the simple case of a homogeneous deformation field, where the gradient of the Cosserat strain tensor and the torsion-curvature tensor $\boldsymbol{\kappa}$ are both equal to zero, because this will be generally assumed in the fault-slip data analysis for the sake of simplicity. First, the second- and third-order projection tensors $\mathbf{N}$ and $\underline{\mathbf{T}}$ are defined with the fourth-order identity tensor $[\underline{\mathbf{1}}]_{ijkl} = \delta_{ik}\delta_{jl}$ and the normal vector to the microplane (fault) $\vec{n}$ as (e.g. Etse and Nieto, 2004):

$$\mathbf{N} = \vec{n} \otimes \vec{n}, \qquad \underline{\mathbf{T}} = \vec{n} \cdot \underline{\mathbf{1}} - \vec{n} \otimes \vec{n} \otimes \vec{n}. \tag{12}$$

In the case of $\boldsymbol{\kappa} = 0$ the direction of slip along the fault is parallel to the resolved shear direction, which is the tangential component of the strain vector:

$$\gamma_i \vec{m_i} = L\underline{\mathbf{T}} : \mathbf{e}. \tag{13}$$

Here, $\vec{m}_i$ represents the unit vector in the direction of slip along the fault, γ_i is the amount of slip, and L is the distance between the centroids of the two neighboring blocks. Because the Cosserat strain tensor depends on the macrodeformation and the relative microrotation tensors, the slip along the fault can be decomposed into two components:

$$\gamma_i \vec{m_i} = \gamma_i^s \vec{s_i} + \gamma_i^c \vec{c_i}. \tag{14}$$

where $\gamma_i^s \vec{s} = L\underline{\mathbf{T}}: u^{(S)}$ represents the contribution of the macro-deformation field to the slip direction along the fault, while $\gamma_i^c \vec{c} = L\underline{\mathbf{T}}: \mathbf{A}$ represents the contribution of the relative microrotations.

4. The stress measures

The classical continuum theory is based on the assumption that the transfer of load between two neighboring material points occurs only through a force vector, leading to the definition of symmetric stress and strain tensors (Onck, 2002). In the Cosserat theory it is, however, assumed that the transfer of the interaction between two particles of the body through a surface element $\vec{n}dS$ occurs not only by means of a traction vector $\vec{\sigma}dS$, but also by means of a moment vector $\vec{\mu}dS$ (e.g. Forest, 2000). Surface forces and couples are then represented by the generally non-symmetric tensors, the force stress tensor $\boldsymbol{\sigma} = \sigma_{ij}$ and the couple-stress tensor $\boldsymbol{\mu} = \mu_{ij}$:

$$\vec{\sigma} = \boldsymbol{\sigma}\vec{n} \quad \text{and} \quad \vec{\mu} = \boldsymbol{\mu}\vec{n}. \tag{15}$$

The force stress vector and the couple-stress vector can be decomposed into normal and tangential components:

$$\vec{\sigma_n} = \mathbf{N}:\boldsymbol{\sigma}, \quad \vec{\tau} = \underline{\mathbf{T}}:\boldsymbol{\sigma}, \quad \vec{\mu_n} = \mathbf{N}:\boldsymbol{\mu}, \quad \vec{\mu_t} = \underline{\mathbf{T}}:\boldsymbol{\mu}. \tag{16}$$

Thus, $\vec{\sigma}_n$ and $\vec{\mu}_n$ represent the normal projected stress and the normal projected couple-stress, whereas $\vec{\tau}$ and $\vec{\mu}_t$ represent the shear stress vector and the tangential projected couple-stress vector, respectively.

The force and couple-stress tensors $\boldsymbol{\sigma}$ and $\boldsymbol{\mu}$ must fulfill the equations of balance of momentum and of balance of moment of momentum:

$$\boldsymbol{\sigma}\cdot\vec{\nabla} + \vec{f} = \rho\ddot{\vec{u}}, \qquad \boldsymbol{\mu}\cdot\vec{\nabla} - \underline{\varepsilon}:\boldsymbol{\sigma} + \vec{c} = I\ddot{\vec{\phi}}, \tag{17}$$

where volume forces $\vec{f}$, volume couples $\vec{c}$, mass density ρ, and isotropic rotational inertia I have been introduced (Forest, 2000).

5. Constitutive equations

The required characteristics of constitutive equations for faulting-related deformation of the Earth's crust (cataclastic flow) were discussed by Twiss and Unruh (1998), who recognized three principal driving mechanisms that should be incorporated: (1) the elastic properties of the blocks bounded by the faults; (2) frictional sliding on shear surfaces (fault planes); and (3) plastic deformation and brittle fracture of rocks. They did not, however, provide an exact mathematical treatment of the problem. Here, we present the constitutive model based on the *J-2* plasticity theory.

Assuming strain is small, the total deformation and curvature tensors can be decomposed into elastic and plastic parts (e.g. Willam, 2002; Forest and Sievert, 2003):

$$\mathbf{e} = \mathbf{e}_e + \mathbf{e}_p, \quad \boldsymbol{\kappa} = \boldsymbol{\kappa}_e + \boldsymbol{\kappa}_p. \tag{18}$$

In the description of the cataclastic flow, we assume that $\mathbf{e}_e \ll \mathbf{e}_p$ and $\boldsymbol{\kappa}_e \ll \boldsymbol{\kappa}_p$, so $\mathbf{e} \approx \mathbf{e}_p$ and $\boldsymbol{\kappa} \approx \boldsymbol{\kappa}_p$. As discussed by Forest and Sievert (2003), the classical theory of so-called standard materials proposed by Germain et al. (1983), Lemaitre and Chaboche (1994), and Forest et al. (2001) can be extended to Cosserat media by presentation of a viscoplastic potential $\Omega(\boldsymbol{\sigma}, \boldsymbol{\mu}, R)$, the so-called pseudo-potential of dissipation, such that:

$$\dot{\mathbf{e}}_p = \frac{\partial\Omega}{\partial\boldsymbol{\sigma}}, \quad \dot{\boldsymbol{\kappa}}_p = \frac{\partial\Omega}{\partial\boldsymbol{\mu}}, \quad \dot{q} = \frac{\partial\Omega}{\partial R}. \tag{19}$$

The thermodynamic force associated with the material internal variable q was denoted by R (see Forest and Sievert, 2003, for a more detailed definition). To ensure the positivity of the intrinsic dissipation, the potential $\Omega(\boldsymbol{\sigma}, \boldsymbol{\mu}, R)$ should be a convex function of its variables. The potential is a coupled function of force and couple stresses, $\Omega(\boldsymbol{\sigma}, \boldsymbol{\mu}, R)$, and can be used to describe rate-independent material behavior. It involves a single yield function $f(\boldsymbol{\sigma}, \boldsymbol{\mu}, R)$ and a single plastic multiplier $\dot{p}$:

$$\dot{\mathbf{e}}_p = \dot{p}\frac{\partial f}{\partial\boldsymbol{\sigma}}, \quad \dot{\boldsymbol{\kappa}}_p = \dot{p}\frac{\partial f}{\partial\boldsymbol{\mu}}, \quad \dot{q} = -\dot{p}\frac{\partial f}{\partial R}. \tag{20}$$

The yielding occurs when (plastic yield condition) $f(\boldsymbol{\sigma}, \boldsymbol{\mu}, R) \le 0$ (Willam, 2002). To derive the constitutive equations for the cataclastic flow, we are interested in the exact formulation of the yield function. In the literature, numerous yield functions have been proposed, which are mainly modifications and extensions of the Mohr–Coulomb, von Mises and Drucker–Prager yield functions (e.g. de Borst, 1991, 1993; Mohan et al., 1999; Hansen et al., 2001; Manzari, 2004; Salari et al., 2004). The onset of yielding of the Cosserat medium can be successfully accounted for using the extended von Mises or Drucker–Prager yield functions (*J-2* plasticity), as discussed, for example, by Sawczuk (1967), Lippmann (1969), Besdo (1974, 1985), Mühlhaus and Vardoulakis (1987), de Borst (1991, 1993), and Forest and Sievert (2003):

$$f(\boldsymbol{\sigma}, \boldsymbol{\mu}, R) = J_{2d}(\boldsymbol{\sigma}, \boldsymbol{\mu}) - R(p) = 0 \tag{21}$$

with:

$$J_{2d}(\boldsymbol{\sigma}, \boldsymbol{\mu}) = \sqrt{a_1\boldsymbol{\sigma}^d:\boldsymbol{\sigma}^d + a_2\boldsymbol{\sigma}^d:\boldsymbol{\sigma}^{dT} + b_1\boldsymbol{\mu}^d:\boldsymbol{\mu}^d + b_2\boldsymbol{\mu}^d:\boldsymbol{\mu}^{dT}}. \tag{22}$$

J_{2d} represents the generalized second invariant of deviatoric stress and couple-stress tensors extended to the Cosserat continuum (de Borst, 1993). $\boldsymbol{\sigma}^d$ is the deviatoric part of the stress tensor, $\boldsymbol{\sigma}^{dT}$ is the transposed deviatoric part of the stress tensor, $\boldsymbol{\mu}^d$ is the deviatoric part of the couple-stress tensor, $\boldsymbol{\mu}^{dT}$ is the transposed deviatoric part of the couple-stress tensor, and a_1, a_2, b_1 and b_2 are the material parameters. Note that the stress tensor $\boldsymbol{\sigma}$ can be decomposed into the spherical and deviatoric parts $\boldsymbol{\sigma} = \boldsymbol{\sigma}^{\bigcirc} + \boldsymbol{\sigma}^d$ with $\boldsymbol{\sigma}^{\bigcirc} = \langle\boldsymbol{\sigma}\rangle = (1/3)\mathrm{Tr}(\boldsymbol{\sigma})\mathbf{1}$ and $\boldsymbol{\sigma}^d = \boldsymbol{\sigma} - \boldsymbol{\sigma}^{\bigcirc}$. The trace of the stress tensor $\mathrm{Tr}(\boldsymbol{\sigma})$ is also known as the first invariant J_1 of the stress. From Eq. (20) we have:

$$\dot{\mathbf{e}}_p = \dot{p}\frac{\partial f}{\partial\boldsymbol{\sigma}} = \dot{p}\frac{a_1\boldsymbol{\sigma}^d + a_2\boldsymbol{\sigma}^{dT}}{J_{2d}(\boldsymbol{\sigma}^d)}. \tag{23}$$

This, of course, is not the most general case, since the couple-stress tensor was neglected. The use of a consistency condition $\dot{f} = 0$ for plastic loading leads to the expression for the plastic multiplier $\dot{p}$, which in this case linearly depends on the rate-of-strain $\dot{\mathbf{e}}_p$ (e.g. Iordache and Willam, 1998; Forest and Sievert, 2003):

$$\dot{p} = \sqrt{\frac{a_1}{a_1^2 - a_2^2}\dot{\mathbf{e}}_p:\dot{\mathbf{e}}_p + \frac{a_2}{a_2^2 - a_1^2}\dot{\mathbf{e}}_p:\dot{\mathbf{e}}_p^T}. \tag{24}$$

Eq. (23) can be rewritten into the following form:

$$\dot{\mathbf{e}}_p = \frac{\dot{p}}{J_{2d}(\boldsymbol{\sigma}^d)}(a_1 + a_2)\boldsymbol{\sigma}^{(S,d)} + \frac{\dot{p}}{J_{2d}(\boldsymbol{\sigma}^d)}(a_1 - a_2)\boldsymbol{\sigma}^{(A,d)} \tag{25}$$

where $\boldsymbol{\sigma}^{(S,d)}$ is the symmetric part of the stress deviator and $\boldsymbol{\sigma}^{(A,d)}$ is the skew-symmetric part of the stress deviator. From this equation it also follows that the following relations hold for the symmetric

and skew-symmetric parts of the deviatoric part of the Cosserat strain tensor:

$$\dot{\mathbf{e}}_p^{(S)} = \frac{\dot{p}}{J_{2d}(\boldsymbol{\sigma}^d)}(a_1+a_2)\boldsymbol{\sigma}^{(S,d)},$$

$$\dot{\mathbf{e}}_p^{(A)} = \frac{\dot{p}}{J_{2d}(\boldsymbol{\sigma}^d)}(a_1-a_2)\boldsymbol{\sigma}^{(A,d)}. \quad (26)$$

Putting this into Eq. (25), we obtain:

$$\dot{\boldsymbol{\sigma}}^d = \dot{\boldsymbol{\sigma}}^{(S,d)} + \dot{\boldsymbol{\sigma}}^{(A,d)} = \frac{J_{2d}(\boldsymbol{\sigma}^d)}{\dot{p}(a_1+a_2)}\dot{\mathbf{e}}_p^{(S)} + \frac{J_{2d}(\boldsymbol{\sigma}^d)}{\dot{p}(a_1-a_2)}\dot{\mathbf{e}}_p^{(A)}, \quad (27)$$

Note that $J_{2d}(\boldsymbol{\sigma}^d) = R(p)$ (Eq. (21)). Now the constitutive equation can be derived. By adding the hydrostatic pressure term $p_r\mathbf{1}$ we see the full stress tensor is:

$$\boldsymbol{\sigma} = p_r\mathbf{1} + a\dot{\mathbf{e}}_p^{(S)} + b\dot{\mathbf{e}}_p^{(A)}, \quad (28)$$

with $a = R(p)/\dot{p}(a_1+a_2)$ and $b = R(p)/\dot{p}(a_1-a_2)$ as the constitutive parameters. It is important that the same constitutive relation as Eq. (28) can also be derived for other yield functions within the *J-2* plasticity model, for example, for the Drucker–Prager yield function (see, for example, de Borst, 1993; Hansen et al., 2001, for the definition) and for the Pitman–Schaeffer–Gray–Stiles yield function (Dartevelle, 2003). In this case, the choice of the yield function only affects the definitions of the constitutive parameters a, b and $p_r\mathbf{1}$, whilst the general shape of the constitutive equation remains the same.

Although the constitutive relation (Eq. (28)) is formulated in terms of rates-of-deformation, in practice we interpret these rates to be represented by small increments of deformation that accumulate over a finite, but geologically very short time intervals (e.g. Twiss and Unruh, 2007). On the assumption that the rate-of-deformation is approximately constant during the deformation phase, the time can be eliminated from the constitutive equation by multiplying it by Δt, which does not affect the result. Thus, the rates are represented by instantaneous deformation, and the time interval, over which these increments accumulate, is not a factor in the analysis. In the fault-slip data analysis, the Cosserat strain tensor and the corresponding stress tensor of the form $\mathbf{e} = konst\cdot\mathbf{e}^{(orig.)}$ and $\boldsymbol{\sigma} = konst\cdot\boldsymbol{\sigma}^{(orig.)}$ are generally calculated, where $\mathbf{e}^{(orig.)}$ and $\boldsymbol{\sigma}^{(orig.)}$ are the actual Cosserat strain and corresponding stress tensors at the time of faulting and $\mathbf{e}$ and $\boldsymbol{\sigma}$ are our solutions, while *konst.* is some undetermined constant. Therefore, the final form of the constitutive equation used in the T-TECTO computer program is:

$$\boldsymbol{\sigma} = p_r\mathbf{1} + a\mathbf{u}^{(S)} + b\mathbf{A} \quad (29)$$

or also

$$\boldsymbol{\sigma} = (1-b)T\cdot\mathbf{1} + (1-b)\mathbf{u}^{(S)} + b\mathbf{A}. \quad (30)$$

Note that $\mathbf{u}^{(S)} = \mathbf{e}_p^{(S)}$ and $\mathbf{A} = \mathbf{e}_p^{(A)}$. Because the tensors of the form $\boldsymbol{\sigma} = konst\cdot\boldsymbol{\sigma}^{(orig.)}$ and $\mathbf{e} = konst\cdot\mathbf{e}^{(orig.)}$ are only determined in the fault-slip data analysis, we may choose $a+b=1$. In addition, the first parameter p_r on the right side of Eq. (29) is defined as $(1-b)T$, with T being some parameter. In this way, the stress tensor $\boldsymbol{\sigma}$ is directly proportional to the Cosserat strain tensor $\mathbf{e}$, when we choose $b = 0.5$:

$$\boldsymbol{\sigma} = (1-b)\left[T\mathbf{1} + \mathbf{u}^{(S)} + \frac{b}{1-b}\mathbf{A}\right] = \frac{1}{2}\left[T\mathbf{1} + \mathbf{u}^{(S)} + \mathbf{A}\right]$$
$$= \frac{1}{2}[T\mathbf{1} + \mathbf{e}]. \quad (31)$$

6. Mohr representation of stress

In a classical continuum, the stress is conveniently represented by the Mohr circles diagram in the Mohr stress space of normal stresses versus shear stresses. The generalization of the Mohr circles diagram to the Cosserat continuum was discussed in detail for the two-dimensional case by, for example, Iordache and Willam (1998), Willam and Iordache (2001) and Figueiredo et al. (2004), so the concept of Mohr diagrams for the Cosserat continuum will be presented here only briefly. The geometrical representation of non-symmetric stress (Fig. 3) results in the generalization of the traditional Mohr circle construction in the following way (Iordache and Willam, 1998; Willam and Iordache, 2001):

$$(\sigma_n - \sigma_c)^2 + (\tau - \tau_c)^2 = r^2, \quad (32)$$

with

$$\sigma_c = \frac{\sigma_{11}+\sigma_{22}}{2}, \quad \tau_c = \frac{\sigma_{12}+\sigma_{21}}{2} \quad \text{and}$$
$$r^2 = \left(\frac{\sigma_{11}-\sigma_{22}}{2}\right)^2 + \left(\frac{\sigma_{12}+\sigma_{21}}{2}\right)^2. \quad (33)$$

Here, σ_{ij} are the components of the stress tensor in the two-dimensional case, σ_n is the normal stress, τ is the shear stress, and σ_c and τ_c represent the position of the center of the Mohr circle with radius r (Fig. 3). The center of the Mohr circle is no longer located on the σ_n coordinate axis. The shift of the center is a measure of the loss of symmetry (Willam and Iordache, 2001). The eigenvalues

$$\sigma_{1,2} = \sigma_c \pm \sqrt{\frac{1}{4}(\sigma_{11}-\sigma_{22})^2 + \sigma_{12}\sigma_{21}} \quad (34)$$

are the principal stresses with zero shear stress. They remain real-valued only as long as the discriminant is positive. When the eigenvalues turn complex conjugate, then the Mohr circle no longer intersects the σ_n coordinate axis, and thus has no real-valued principal stresses. It is also important to note from the Mohr diagram (Fig. 3) that the shear stress on planes with maximal normal stress is not zero in such cases.

The construction of the Mohr diagram for the three-dimensional case is more complex. We are not aware of any general theory for analytical construction of Mohr diagrams for three-dimensional asymmetric matrices. Therefore, in the T-TECTO computer program the three-dimensional Mohr diagrams for the Cosserat continuum are constructed numerically by plotting the area of possible values of normal and shear stress in gray color. Fig. 4 shows Mohr diagrams for three different values of the relative microrotation

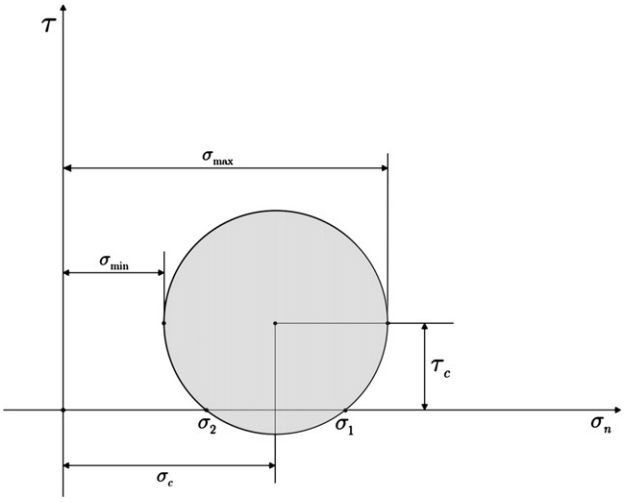

Fig. 3. The Mohr circle of non-symmetric state of plane stress. Simplified after Willam and Iordache (2001). See text for details.

parameter W and constitutive parameters a and b. For small values of the parameters W and b the Mohr diagram looks similar to the classical case (Fig. 4b). In this case, three eigenvalues exist which define the orientation of planes with zero shear stress. For larger values of the parameters W and b, however, Mohr diagrams become more complex and do not necessarily define three zero shear stress planes, but only two or even a single one (Fig. 4c). In this last case, two eigenvalues of the stress tensor are complex conjugate, and the third is real.

7. Fault reactivation in the Cosserat continuum

Finally, we can derive equations for fault reactivation in the Cosserat continuum. In the classical continuum the condition for reactivation would be given by Amontons's Law (e.g. Jaeger and Cook, 1969; Reches, 1978, 1983; Angelier, 1989; Ranalli and Yin, 1990; Reches et al., 1992; Yin and Ranalli, 1992, 1995; Udias, 1999; Ranalli, 2000; Fry, 2001):

$$\tau \geq \mu\sigma_n = \sigma_n \cdot \tan\phi_2, \tag{35}$$

where $\sigma_n = \|\mathbf{N}\colon \boldsymbol{\sigma}\|$ is the normal stress acting on the fault, $\vec{\tau} = \underline{\mathbf{T}}\colon \boldsymbol{\sigma}$ is the resolved shear stress, and μ and ϕ_2 are the coefficient and angle of residual friction for sliding on the pre-existing fault, respectively. Amontons's Law states that the fault is (re)activated when the resolved shear stress exceeds the frictional shear strength of the fault. In a similar way, the formation of new faults is explained, for example, by the Coulomb–Mohr criterion $\tau = S_0 + \sigma_n \cdot \tan\phi_i$, where S_0 is the cohesion, and ϕ_i is the angle of internal friction. New faults are formed when the largest Mohr circle on the Mohr diagram touches the line $\tau = S_0 + \sigma_n \cdot \tan\phi_i$ (e.g. Jaeger and Cook, 1969; see also Fig. 4).

In the Cosserat continuum, the above condition (Eq. (35)) is not enough for a fault to be (re)activated. The direction of slip along the fault is given by equation $\gamma_i \vec{m}_i = L\underline{\mathbf{T}}\colon \mathbf{e}$ (Eq. (13)) and depends on the Cosserat strain tensor (supposing that the torsion-curvature tensor can be neglected). Because of the nonlinear constitutive relationship between the stress and strain, the shear stress $\vec{\tau} = \underline{\mathbf{T}}\colon \boldsymbol{\sigma}$ is generally non-parallel to the direction of movement. In addition, the traction of the two neighboring blocks is also related to a couple-stress, with a normal component $\vec{\mu}_n = \mathbf{N}\colon \boldsymbol{\mu}$ and a tangential component $\vec{\mu}_t = \underline{\mathbf{T}}\colon \boldsymbol{\mu}$. Generalization of the Amontons's condition, Eq. (35), to the Cosserat continuum would be:

$$\left(\vec{\tau} + \frac{1}{L_c}\vec{\mu_t}\right)\cdot\vec{m} \geq \mu\left(\sigma_n + \frac{1}{L_c}\mu_n\right) \quad \text{or}$$

$$\left(\underline{\mathbf{T}}\colon\boldsymbol{\sigma} + \frac{1}{L_c}\underline{\mathbf{T}}\colon\boldsymbol{\mu}\right)\cdot\vec{m} \geq \mu\left(\|\mathbf{N}\colon\boldsymbol{\sigma}\| + \frac{1}{L_c}\|\mathbf{N}\colon\boldsymbol{\mu}\|\right). \tag{36}$$

Here L_c represents characteristic length for the torsion-curvature in the Cosserat medium. In some cases, we expect that L_c could be of the same order of magnitude as the distance between the centroids of the two neighboring blocks L. In the case of homogeneous deformation of the Cosserat medium, the torsion-curvature tensor $\boldsymbol{\kappa}$ remains small, because it depends on the gradient of the Cosserat strain tensor $\mathbf{e}$ (Eq. (4)). This also means that the couple stresses can be neglected and the Amontons's condition for fault reactivation depends only on the stress tensor $\boldsymbol{\sigma}$:

$$(\underline{\mathbf{T}}\colon\boldsymbol{\sigma})\cdot\vec{m} \geq \mu\|\mathbf{N}\colon\boldsymbol{\sigma}\| \quad \text{or} \quad \tau^r = \vec{\tau}\cdot\vec{m} \geq \mu\sigma_n. \tag{37}$$

A fault can be activated when the Mohr point on the Mohr diagram, illustrating the values of normal stress and shear stress component in the direction of movement τ^r, lies above the straight line $\tau \geq \mu\sigma_n$, which represents Amontons's Law of Friction (Fig. 4). It is important to note that based on the proposed constitutive equation (Eqs. (28) or (29)) the skew-symmetric component of stress tensor affects only the magnitude of shear stress. Since $\mathbf{A}\vec{n} = \mathbf{e}^{(A)}\vec{n} = \vec{\phi}^{rel}\times\vec{n}$, we have:

$$\boldsymbol{\sigma}\vec{n} = p_r\vec{n} + a\mathbf{e}^{(S)}\vec{n} + b\mathbf{e}^{(A)}\vec{n} = p_r\vec{n} + a\mathbf{e}^{(S)}\vec{n} + b\vec{\phi}^{\,\mathrm{rel}}\times\vec{n}. \tag{38}$$

The vector $\mathbf{A}\vec{n} = \mathbf{e}^{(A)}\vec{n} = \vec{\phi}^{rel}\times\vec{n}$ is perpendicular to the normal vector $\vec{n}$ and, consequently, the contribution of the skew-symmetric component of the stress tensor lies in the fault plane. The shear stresses in the asymmetric stress regimes will therefore be higher than in symmetric stress regimes.

In Fig. 5 we illustrate how the possible orientations of slip-capable faults are influenced by varying boundary conditions defined by the Cosserat strain tensor and the corresponding stress tensor. Faults were generated with the AmontonsWin computer

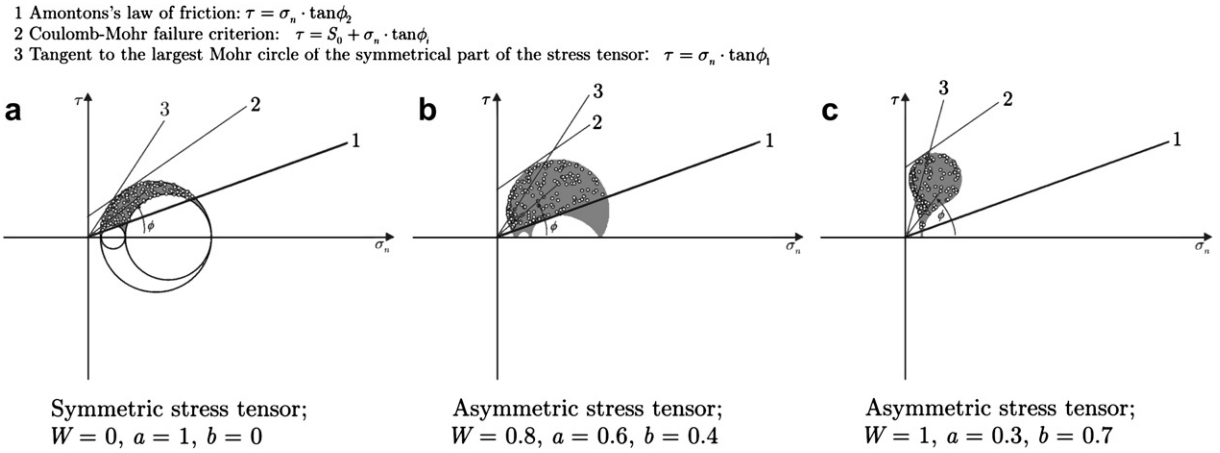

Fig. 4. Mohr circles for non-symmetric states of stress (three-dimensional case) for various values of constitutive parameters a and b. (c) represents the most asymmetric stress tensor. Activation of faults in symmetric and non-symmetric states of stress is possible, whenever the Mohr point (illustrating the value of normal stress and shear stress component in the direction of movement along a fault) lies above the line $\tau = \sigma_n \cdot \tan\phi_2$ representing Amontons's Law of Friction. The line $\tau = S_0 + \sigma_n \cdot \tan\phi_i$ represents Coulomb–Mohr failure criterion (Jaeger and Cook, 1969). S_0 is the cohesion and ϕ_i is the angle of internal friction. The line $\tau = \sigma_n \cdot \tan\phi_1$ represents the tangent to the largest Mohr circle (for the symmetric part of the stress tensor). ϕ is the angle of friction for the individual fault. See text for details.

program, which is part of the T-TECTO 2.0 suite. AmontonsWin generates a prescribed number of faults, which are either randomly orientated or follow a pre-defined distribution of orientations. The direction of slip along the faults is then set parallel to the resolved shear direction on the fault planes, calculated from the input Cosserat strain tensor according to the equation $\gamma_i \vec{m}_i = L\underline{\mathbf{T}} : \mathbf{e}$ (Eq. (13)). The faults can only be activated when the resolved remote shear stress in the direction of slip exceeds the frictional resistance for sliding according to Amontons's Law. Even from the randomly generated population of faults, only the faults with mechanically suitable orientation are accepted by the AmontonsWin program, thus providing insights into possible geometries of slip-capable fault systems under various stress–strain boundary conditions. The boundary conditions in the experiments shown in Fig. 5 were controlled by varying the parameters a, b, W and ϕ_2. The following can be deduced:

1. The experiment in Fig. 5a demonstrates a classical case with no relative microrotations. The relative microrotation parameter was set to $W = 0$ and, consequently, the relative microrotation tensor **A** also equals zero. The possible slip-capable fault system is symmetrical with respect to the principal strain axes of the macrostrain tensor, producing conjugate or orthorhombic geometry. Such fault systems accommodate a non-rotational bulk deformation.
2. In the experiment in Fig. 5b, relative microrotations were introduced, with $W = 1$, $a = 0.5$, $b = 0.5$, $p_r = 0.22$, and $\phi_2 = 30^\circ$. In this case the stress tensor is directly proportional to the Cosserat strain tensor (Eq. (31)) and consequently the direction of shear calculated from the Cosserat strain tensor is parallel to the shear stress calculated from the stress tensor. The slip-capable fault system in such boundary conditions is clearly non-symmetrical with respect to the principal strain axes of the macrostrain tensor. This example shows that the relative microrotation not only affects the direction of slip along the faults, but also affects the geometry of the activated fault system which accommodates the applied strain and stress boundary conditions.
3. The experiment in Fig. 5c illustrates the effect of relative microrotations on the direction of slip along the faults. We generated a north-dipping and a south-dipping fault set. The parameter values were set to $a = 0.5$, $b = 0.5$, $p_r = 0.22$, and the angle of residual friction was set to $\phi_2 = 30^\circ$. In the classical case with no relative microrotation ($W = 0$), all faults exhibit reverse slip. When, however, relative microrotations are present, the slip on the faults becomes reverse-oblique.
4. The experiment in Fig. 5d shows that in the case of large relative microrotations ($W = -1$) coupled with asymmetric stress states ($a = 0.5$, $b = 0.5$, $p_r = 0.13$) both very steeply and very gently dipping reverse and normal faults can be activated, even when the angle of residual friction is set to the "normal" value $\phi_2 = 30^\circ$. In this case the faults are almost perpendicular to one of the principal strain axes of the macrostrain tensor. In a classical continuum model, slip activation on such faults would only be possible if friction was very low.
5. Fig. 5e shows two theoretical fault systems generated in the symmetric and asymmetric stress state and in the strain boundary conditions characterized by intensive relative microrotation. The fault system geometry formed in an asymmetric stress state differs significantly from that formed in

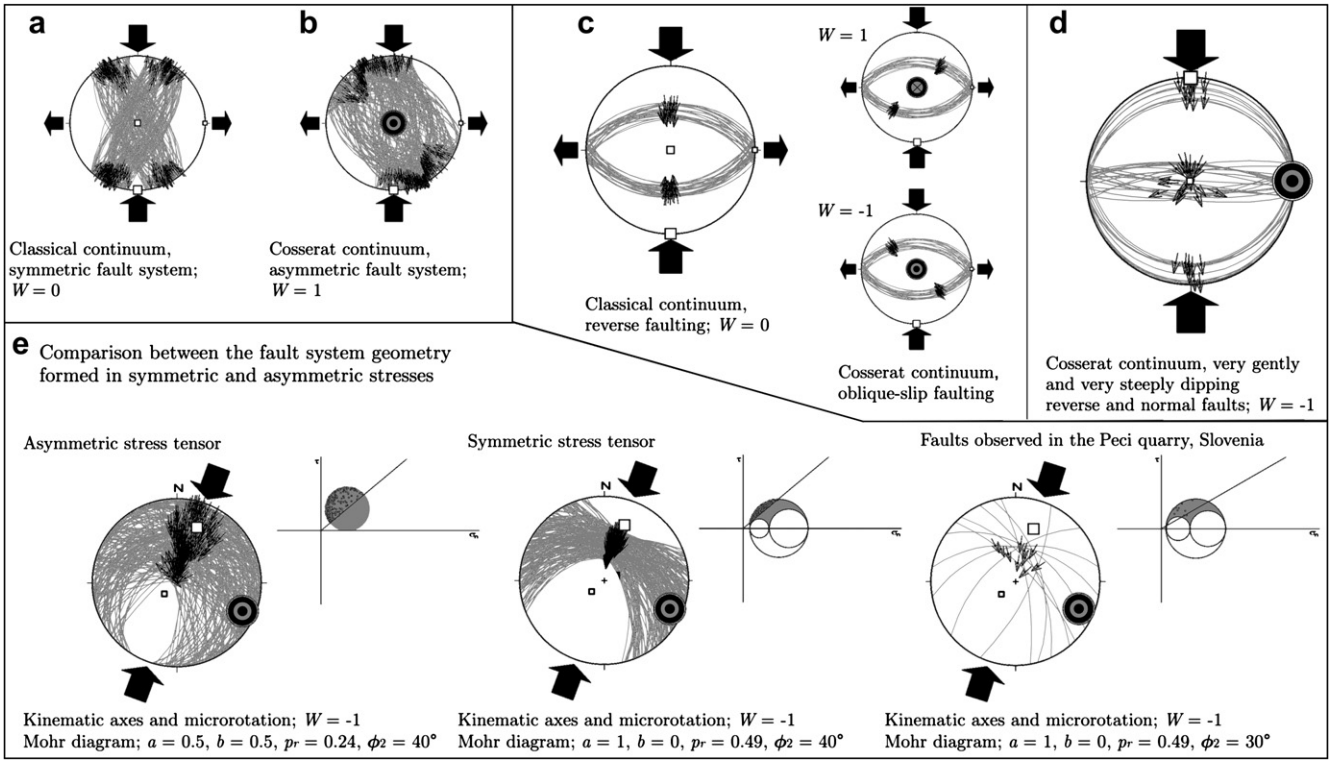

Fig. 5. Forward modeling of possible fault orientations: (a) in a classical continuum; and (b) in a Cosserat continuum. The fault system is symmetrical for the case of zero relative microrotation, but becomes asymmetrical (with respect to the principal strain axes of the macrostrain tensor) with increasing relative microrotation. (c) Shows the effect of relative microrotations on the direction of slip along the faults. (d) Shows that in the Cosserat continuum the faults in unsuitable orientation with respect to the principal strain axes of the macrostrain tensor can be activated without the requirement for low residual friction. (e) Theoretical fault system geometry in symmetric and asymmetric stress states and in the strain field characterized by intensive relative microrotation. (e) Also shows one illustrative natural example observed in the Upper Triassic limestone in the Peci quarry (lat = 46°17′46″, lon = 14°12′51″) in Slovenia, with a geometry remarkably similar to that predicted by the theory for symmetric stress. See text for details.

a symmetric stress. In the case of symmetric stress, all the faults are inclined at approximately the same angle with respect to the horizontal plane, while the slip direction along the faults tends to be sub-parallel to the common intersection between the fault planes. Our field observations show that natural fault systems often exhibit such geometry. Fig. 5e shows such a natural fault system, observed in the Upper Triassic limestone in the Peci quarry, Slovenia. Its geometry is remarkably similar to that predicted by the Cosserat theory for symmetric stress.

8. Cosserat stress–strain inverse modeling

One of the main goals of fault-slip data analysis is to find the stress and/or strain tensor, capable of explaining the direction of slip on most of the faults observed in the studied rock mass. Generally, this problem is referred to by structural geologists as *the inverse problem* (Fleischman and Nemcok, 1991; Angelier, 1994; Twiss and Unruh, 1998). We extended the Gauss paleostress inverse method (Žalohar and Vrabec, 2007) to the Cosserat continuum. The Gauss paleostress method defines the *compatibility measure* and *compatibility function*, which verify the compatibility of a given stress tensor with observed fault-slip data. In the classical paleostress analysis, it is assumed that the direction of slip along the fault is parallel to the resolved remote shear stress acting along that fault. The compatibility of a chosen fault is therefore related to the angular misfit α_i between the actual direction of slip and the theoretical direction of shear stress. In the Cosserat stress–strain analysis of fault-slip data, the direction of slip along the faults no longer reflects the direction of shear stress, but is parallel to the shear associated with the large-scale deformation boundary conditions defined by the Cosserat strain tensor. It is assumed that the direction of slip is defined by Eq. (13): $\gamma_i \vec{m}_i = L\underline{\mathbf{T}}:\mathbf{e}$. The compatibility of a given fault therefore depends on the Cosserat strain tensor and not on the stress tensor. At the same time, however, it is assumed that the fault can only be active when the resolved remote shear stress in the direction of slip $\tau^r = (\underline{\mathbf{T}}:\boldsymbol{\sigma})\cdot\vec{m}$ exceeds the frictional resistance for sliding $\mu\|\mathbf{N}:\boldsymbol{\sigma}\|$ (see Eq. (37)). Thus, fault-slip data contain information on both the Cosserat strain tensor and stress tensor, which have to be extracted in the inverse modeling.

The optimal solution for the Cosserat strain tensor and the corresponding stress tensor associated with the observed faults can be found by searching for the global and highest local maxima of the *object function* F_0 defined as a sum of *compatibility functions* for all fault-slip data. First, we define the *compatibility measure*, which considers both the angular misfit α_i between the predicted and actual direction of slip on the fault, and the position of the "Mohr point" on the Mohr diagram:

$$\delta_i^2 = \alpha_i^2 + \left(w_{2,i}|\phi-\phi_2|\frac{2\Delta}{\phi_2}\right)^2 + \left(w_{1,i}|\phi-\phi_1|\frac{2\Delta}{\phi_1}\right)^2, \tag{39}$$

where parameters $w_{1,i}$ in $w_{2,i}$ are as follows:

$$\begin{aligned} w_{2,i} &= 1, \quad \text{when } \phi < \phi_2, \\ w_{2,i} &= 0, \quad \text{when } \phi \geq \phi_2 \end{aligned} \tag{40}$$

and

$$\begin{aligned} w_{1,i} &= 1, \quad \text{when } \phi > \phi_1, \\ w_{1,i} &= 0, \quad \text{when } \phi \leq \phi_1. \end{aligned} \tag{41}$$

The angle of friction ϕ for an individual fault is measured between the σ_n axis on the Mohr diagram and the line which connects the "Mohr point" and the origin of the Mohr diagram (Fig. 4). The parameters ϕ_1 and ϕ_2 constrain the possible values of the ratio between the normal and shear stress on the faults. The parameter ϕ_2 represents the angle of residual friction for sliding on a pre-existing fault, $\phi_2 = \arctan(\mu)$, and the parameter ϕ_1 roughly approximates the angle of internal friction ϕ_i for the intact rock. Since the angle of internal friction ϕ_i generally has a higher value than the angle of residual friction ϕ_2, the value of the parameter ϕ_1 should also be slightly higher than ϕ_2. When the angle of friction ϕ for the individual fault is outside the range of values between ϕ_1 and ϕ_2, the value of the compatibility measure is increased. In this way the above compatibility measure favors mechanically acceptable solutions to the inverse problem. It is also convenient to use such a definition of the compatibility measure, because in the case of mechanically less compatible faults (small shear stress and high normal stress) small changes in orientation of the fault plane can often result in large changes in orientation of slip direction. The above compatibility measure prevents such faults from influencing the final results of the fault-slip data analysis.

The parameter Δ represents a threshold value for the compatibility measure δ_i. Only the strain and stress tensors that explain the direction of slip on a given fault and position of its "Mohr point" on the Mohr diagram with the compatibility measure δ_i lower than the selected threshold Δ are considered to be compatible with the observed fault-slip datum.

In the Gauss method, we also define the Gaussian *compatibility function*:

$$w_i = \frac{1}{1-\exp\left(-\Delta^2/2s^2\right)}\left(\exp\left(-\frac{\delta_i^2}{2s^2}\right)-\exp\left(-\frac{\Delta^2}{2s^2}\right)\right),$$

$$\text{when } \delta_i < \Delta,$$

$$w_i = 0, \text{ when } \delta_i \geq \Delta. \tag{42}$$

Here, parameter s represents the value of the second moment (dispersion parameter) of the distribution of angular misfit between the predicted and actual direction of slip along the faults. Only the faults that are eventually compatible with the chosen Cosserat strain and stress tensors contribute to the value of the object function F_0, because for such faults the value of the compatibility measure δ_i is small and the value of compatibility function w_i is high. For mechanically and kinematically less compatible faults, the value of the compatibility measure δ_i increases and, consequently, the value of compatibility function w_i decreases. Ideally, for all the outliers, the value of the compatibility function should be zero, since it is supposed that the outliers either belong to different deformation phases in the deformation history of the region, or represent faults influenced by local strain and stress fields. The mathematical aspects of Eq. (42) and the effectiveness of the Gauss inversion method were discussed in detail by Žalohar and Vrabec (2007).

The optimal solution for the Cosserat strain tensor and its associated stress tensor can be found by searching for the global and local maxima of the object function;

$$F_0 = \sum_{i=1}^{N} w_i = \max. \tag{43}$$

Because the direction of slip along the fault is calculated from the Cosserat strain tensor $\mathbf{e}$, and the state of stress along the fault is calculated from the stress tensor $\boldsymbol{\sigma}$, which is related to the Cosserat strain tensor through the constitutive equation (Eq. (29)), the object function depends only on the Cosserat strain tensor, $F_0 = F_0(\mathbf{e}, \boldsymbol{\sigma}(\mathbf{e})) = F_0(\mathbf{e})$. The described procedure finds the Cosserat strain tensor of the form $\mathbf{e} = konst\cdot\mathbf{e}^{(orig.)}$, where $\mathbf{e}^{(orig.)}$ is the actual

Cosserat strain tensor at the time of faulting, **e** is our solution, and *konst*. is some undetermined constant. The stress tensor is calculated from the Cosserat strain tensor with the constitutive equation $\boldsymbol{\sigma} = p_r\mathbf{1} + a\mathbf{u}^{(S)} + b\mathbf{A}$. Note that the obtained stress tensor is also of the form $\boldsymbol{\sigma} = konst \cdot \boldsymbol{\sigma}^{(orig.)}$. A careful inspection of the derived Cosserat stress–strain inverse method shows that the reconstruction of the Cosserat strain tensor and its associated stress tensor depends on the parameters s, Δ, a, b, p_r, ϕ_1, and ϕ_2, which should be set by the user prior to the analysis. The values of the parameters should be chosen as follows:

1. The values of parameters s and Δ depend on the inhomogeneity of the strain/stress field at the time of faulting. When the strain/stress field at the time of faulting is highly inhomogeneous, the values of s and Δ should be large, for example, $s \geq 30^\circ$ and $\Delta \geq 60^\circ$. If the strain/stress field is less inhomogeneous, lower values could be used, for example, $s \geq 15^\circ$ and $\Delta \geq 30^\circ$. The inversion procedure should be repeated many times with different values of the parameters s and Δ in order to find the best strain/stress tensor solutions. The optimal solutions are identified when the calculated standard deviation of angular misfit s_0 and maximum angular misfit α_{max} predicted by the given strain/stress tensor solutions are smaller or approximately equal to the values of s and Δ used in the inversion.
2. The values of the parameters a and b are always between zero and one. For the symmetric stress tensor, the parameter b is equal to zero, and the parameter a is equal to one. For the completely skew-symmetric stress tensor the opposite holds: $a = 0$ and $b = 1$. If we want the stress tensor to be a linear function of the Cosserat strain tensor, we choose $b = 0.5$. The parameter p_r in the constitutive equation is calculated automatically by the T-TECTO with resolution 0.01 to insure the optimal position of the Mohr points on the Mohr diagram: they should lie between the straight lines $\tau = \sigma_n \tan\phi_1$ and $\tau = \sigma_n \tan\phi_2$ (see Fig. 4).
3. The optimal values of the parameters ϕ_1 and ϕ_2 for different rocks and granular materials are documented in literature (e.g. Jaeger and Cook, 1969; Schellart, 2000). The parameter ϕ_2 constrains the lowest possible value for the angle of friction on the pre-existing fault and the parameter ϕ_1 represents the highest possible value for the angle of friction on the pre-existing fault. Since the angle of internal friction ϕ_i generally has a higher value than the angle of residual friction ϕ_2, the value of the parameter ϕ_1 should be slightly higher than ϕ_2. Usually, the best values for these parameters are: $\phi_1 \approx 60^\circ$ and $\phi_2 \approx 30^\circ$.

After the values of the parameters s, Δ, a, b, p_r, ϕ_1, and ϕ_2 are properly chosen, the object function F_0 is maximized by use of the grid-search method. All possible trial Cosserat strain and corresponding stress tensors are calculated in the following way. First, the dip angle of the principal kinematic axis $\vec{\lambda}_1$ is defined, ranging from 2° to 89° with resolution of 5°. For each dip angle, the dip direction is calculated, increasing from 2.5° to 360° at regular intervals of $(90^\circ/(90^\circ - \text{dip})) \cdot 5^\circ$. Second, the $\vec{\lambda}_2$ and $\vec{\lambda}_3$ axes are rotated in the plane perpendicular to each $\vec{\lambda}_1$ axis in the clockwise sense for 180° at regular intervals of 5°. The best values of principal strains λ_1, λ_2 and λ_3 are found by defining the parameter $D = (\lambda_2 - \lambda_1)/(\lambda_3 - \lambda_1)$, which describes the shape of the strain ellipsoid (e.g. Twiss and Unruh, 1998). Because we choose $\lambda_1 \geq \lambda_2 \geq \lambda_3$, the parameter D can range from zero to one. The resolution of the parameter D in the current version of the program T-TECTO is 0.1. We also take $\mathrm{Tr}(\mathbf{u}^{(S)}) = \lambda_1 + \lambda_2 + \lambda_3 = 0$ (no volume changes). In the last step, the relative microrotation parameter W is increased from −1 to 1 with resolution of 0.1. In this way, we first calculate the trial Cosserat strain tensor, while the corresponding stress tensor is calculated from the constitutive equation (Eq. (29)).

In summary, the Cosserat stress–strain inverse method allows us to find the Cosserat strain tensor and associated stress tensor. The stress tensor is used only as a tool for analyzing fault reactivation, while the Cosserat strain tensor defines the orientation of the principal strain axes $\vec{\lambda}_1$, $\vec{\lambda}_2$ and $\vec{\lambda}_3$ (kinematic axes) and the direction and sense of the relative microrotation axis described by $\vec{\phi}^{rel}$ and W. The kinematic axes represent the directions of the largest shortening and extension in the region. It is worth noting that the relative microrotation axis $\vec{\phi}^{rel}$ does not also define the sense of the actual microrotation of blocks between the faults, because the relative microrotation is the difference between the macrorotation and microrotation $\vec{\phi}^{rel} = \vec{\phi}^{macro} - \vec{\phi}^{Cosserat}$.

9. Case study: analysis of fault system at the Sinji vrh experimental site

9.1. Geological setting

In our selected case study we present the analysis of a fault system observed in Jurassic limestone in an underground tunnel at the Sinji vrh experimental site, SW Slovenia (lat = 45°54′27″, lon = 13°55′37″). The site is located in the Cenozoic External Dinarides fold-and-thrust belt (Fig. 6a). The experimental tunnel runs across the regional-scale NW–SE oriented, dextral strike-slip Avče Fault (Veselič et al., 1998). The measured section is 150 m long and is situated in the outer fractured zone of the Avče Fault, immediately adjacent to the 40 m wide cataclastically crushed core zone. The analyzed fault network is a highly asymmetric system of 90 small-scale faults (Fig. 6b), with well-developed slickensides exhibiting good sense-of-shear criteria on fault planes. The prevailing orientation of observed faults is NNW–SSE, almost perpendicular to the main Avče Fault.

Map-scale observations and regional paleostress analysis suggest that the prominent NW–SE oriented faults of SW Slovenia originated as dip-slip normal faults in NE–SW-directed extension, subsequent to the SW-directed thrusting of the Dinarides in the Eocene-Oligocene times (Vrabec and Fodor, 2006). The NW–SE oriented faults consistently cut and displace Dinaric thrust structures and are therefore clearly younger than thrusting.

A later weak oblique-sinistral reactivation during approximately E–W directed shortening is observable at some localities (Gregorič, 2005). Finally, in the post-Miocene strain field characterized by N–S contraction and E–W extension, the kinematics of the NW–SE trending faults was changed to dextral strike-slip (Vrabec and Fodor, 2006).

9.2. Stress–strain inversion of the fault-slip data

Inversion was performed by trying a range of values for the parameters s, Δ, a, b, ϕ_1, and ϕ_2. All results consistently indicate approximately N-S oriented maximum contraction and E–W oriented extension, consistent with the latest, post-Miocene regional kinematic phase (Vrabec and Fodor, 2006). The inversion results also consistently indicate intensive relative microrotations around a subvertical rotation axis, with the relative microrotation parameter W equal to one. Fig. 7 shows two inversion results for two different values of the constitutive parameter b. The employed values of other inversion parameters were $s = 50^\circ$, $\Delta = 70^\circ$, $\phi_1 = 80^\circ$, and $\phi_2 = 30^\circ$. In both cases, the standard deviation s_0 of misfit between the predicted and actual direction of slip along the faults remains under 20°, which indicates a good kinematic compatibility between the data and the determined Cosserat strain tensor. We varied the value of parameter b ranging from zero to one (with resolution of 0.1 and with $a = 1 - b$) to test the mechanical compatibility of the observed fault system with symmetric and asymmetric stress tensors. Fig. 8a shows the

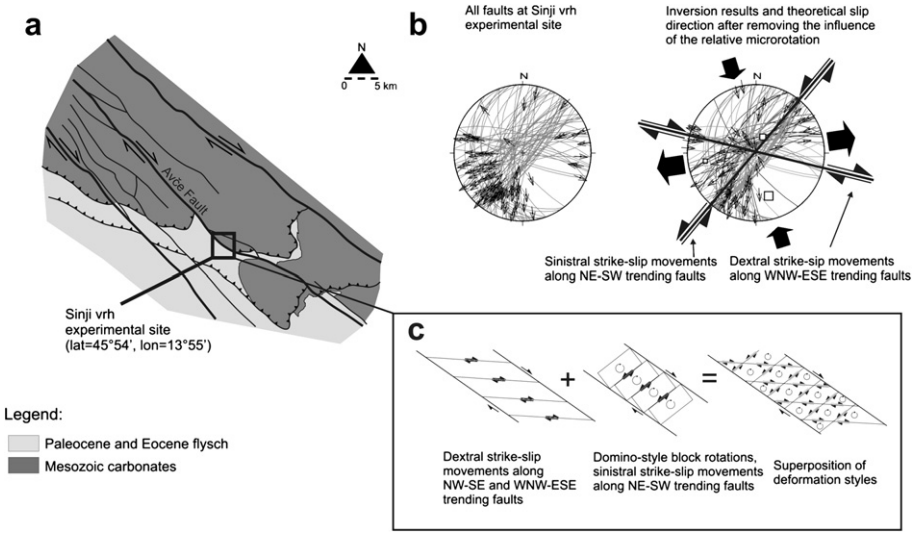

Fig. 6. Structural setting of the fault system at the Sinji vrh experimental site. (a) Geological map of the region (simplified after Janež et al., 1997). (b) The fault system observed at the Sinji vrh experimental site and hypothetical slip directions along the faults after elimination of the effect of the relative microrotation. (c) A simplified structural interpretation of the deformation style. See text for details.

dependence of the number of mechanically and kinematically compatible faults N on the constitutive parameter b. When the symmetric stress tensor is used ($b = 0$), the shear stress component in the direction of movement exceeds proposed frictional resistance for sliding on only 53% of the measured faults, with the remaining fault-slip data being mechanically incompatible with the calculated stress tensor (Figs. 7a and 8a). With higher values of the parameter b, the stress tensor becomes increasingly asymmetrical and the number of mechanically compatible faults rises considerably (Figs. 7b and 8a; see also Eq. (38)). The number of compatible faults reaches its maximum at $b = 0.74$. For $b = 0.7$, there are 81% of faults compatible with the calculated Cosserat strain tensor and the corresponding stress tensor (Fig. 7b). For larger values of b the number of compatible faults drops. For $b = 1$ (completely skew-symmetric stress tensor) no reliable solution was found. Fig. 8b shows another criterion to verify the reliability of the inversion results and the value of parameter b. The best inversion solutions are characterized by a high number of compatible faults N and low values of standard deviation of misfit between predicted and actual direction of slip s_0. Therefore, in Fig. 8b we analyzed the dependence of the ratio N/s_0 on parameter b. The ratio N/s_0 has a distinctive minimum at $b = 2.3$ and reaches its maximum at $b = 0.8$. Comparing results shown in Fig. 8a and b, we find the best value of parameter b is between 0.7 and 0.8.

9.3. Comparison with the forward model

We additionally used the AmontonsWin program to generate an artificial fault system under similar stress and strain boundary conditions to those determined in the inverse procedure. We performed eleven tests using all possible values of the constitutive parameter b ranging from zero to one with resolution of 0.1. The value of the parameter W was always set to one. The geometry of the fault system produced by forward modeling came closest to that observed in nature for $b = 0.5$ (Fig. 9b). In this case, there is a remarkable similarity between the forward model and the geometry of the fault system observed in the field (Figs. 6b and 9a). The direct model, therefore, suggests a slightly smaller value of parameter b than the inverse analysis. Comparing the results of both the direct and inverse models shows that the best value of this parameter can be estimated as $b = 0.7 \pm 0.2$, which suggests that the stress tensor is highly asymmetric.

Our case study clearly demonstrates that where asymmetric stresses are operating, a large number of faults may be compatible with a single kinematic episode, whereas the application of classical fault-slip inversion methods, which intrinsically assume symmetric stress states, might erroneously suggest the existence of several deformation phases.

9.4. Structural interpretation

A structural interpretation of the deformation style is graphically illustrated in Fig. 6b and c. In Fig. 6b, we calculated the hypothetical direction of slip $\overrightarrow{s} = (1/\gamma_i^s) L \underline{\mathbf{T}} : \mathbf{u}^{(S)}$ eliminating the influence of the relative microrotation (see Eq. (14)). This shows that most of the deformation was accommodated by dextral strike-slip movements along WNW–ESE trending faults and sinistral strike-slip movements along NE–SW trending faults. The complete fault system accommodated shortening approximately in the N–S (NNW–SSE to NNE–SSW) direction with strong CW relative microrotations around a subvertical axis (Figs. 7 and 9a). Such a deformation style can be interpreted as a superposition of two deformation mechanisms, which are graphically illustrated in Fig. 6c. The first deformation mechanism is characterized by the interaction between the regional NW–SE trending dextral strike-slip faults (such as the Avče Fault) and the WNW–ESE trending faults which also accommodated dextral strike-slip movements within the fault zone. The second deformation mechanism is characterized by domino-style block rotations, indicating the interaction between the regional NW–SE trending dextral strike-slip faults and smaller NE–SW trending sinistral strike-slip faults. The field of the relative microrotation was defined by this second deformation mechanism. The positive value of the parameter $W = 1$ suggests that the microrotations exceeded the macrorotation, and thus the fault blocks rotated clockwise faster than the macrorotation associated with the (macro)shear along the faults.

10. Discussion

10.1. Constitutive relation between the stress and strain

The cataclastic flow of rocks can be described within the theory of plasticity and frictional flow of granular media extended to the

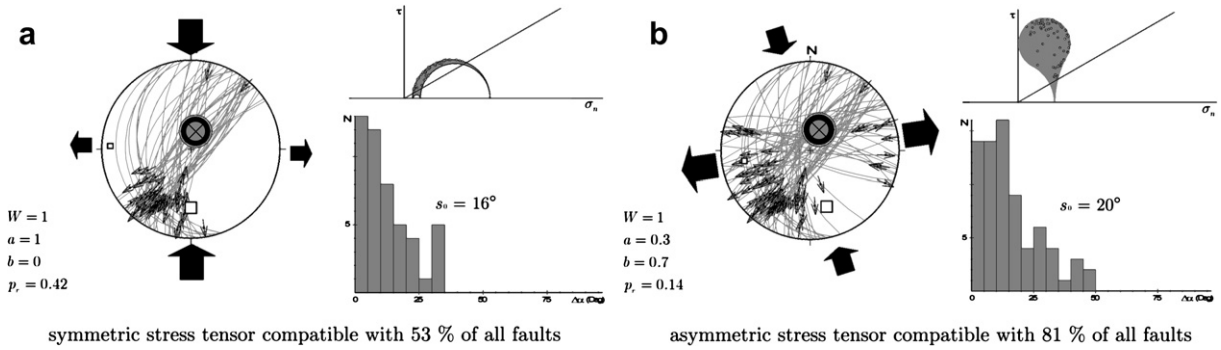

Fig. 7. Results of the Cosserat stress–strain inverse analysis of the Sinji vrh fault system for two different values of inversion parameters. See text for details.

Cosserat continuum by using one of the several possible failure criteria (see, for example, de Borst, 1993; Dai et al., 1996; Dartevelle, 2003; Lubliner, 1990, for a more extensive overview). The extension of the *J-2* plasticity model to the Cosserat continuum that we developed here leads to a constitutive equation in which the symmetric part of the stress tensor depends on the symmetric macrodeformation tensor, whereas the skew-symmetric part of the stress tensor depends on the relative microrotation tensor (Eq. (28)). On closer examination this constitutive equation implies that the stress is first-order rate-of-strain independent. Increasing the rate-of-strain $\dot{\mathbf{e}}_p$ to some degree does not affect the magnitude of the stress, because the material parameters a and b are inversely proportional to the rate-of-plastic multiplier $\dot{p}$, which is also proportional to $\dot{\mathbf{e}}_p$. The derived constitutive equation is therefore nonlinear.

Our numerical simulations performed with the AmontonsWin program demonstrated that in strain fields characterized by non-symmetric Cosserat strain and stress tensors, the geometry of active fault systems is generally also non-symmetrical. The effect of relative microrotations on the geometry of active fault systems was recognized earlier by Twiss et al. (1991, 1993), and Twiss and Unruh (1998, 2007). In this article we have shown that the strain is not the only parameter controlling the geometry of fault systems. The geometry also depends on the stress tensor, which in the Cosserat continuum is usually non-symmetric (Fig. 5). Our *J-2* plasticity model shows that the asymmetry of the stress tensor depends on the relative microrotation tensor and on constitutive parameters a and b. Such a model predicts anisotropic cataclastic flow and formation of asymmetric fault systems with a geometry remarkably similar to that of natural fault systems (Figs. 5e and 9), for both symmetric and asymmetric stresses.

10.2. How do we find the best values of the constitutive parameters a and b ?

The best values of the constitutive parameters a and b, needed in the inversion procedure, can be found in two ways. First, the grid-search method can be performed for all possible values of parameter b ranging from zero to one and with $a = 1 - b$. The best values of these parameters are identified when the object function has the highest value. While this automatic procedure can find a mathematically optimal solution, we do not prefer it, because it does not allow a satisfying structural interpretation. Our recommended workflow is to repeat the inversion procedure for all possible values of parameter b ranging from zero to one with resolution of 0.1 (eleven tests). In this way the numerical stability and dependence of the inversion results on parameters a and b can be directly observed. The best inversion results (the optimal value of parameter b) are characterized by the largest number of kinematically and mechanically compatible faults N and the largest ratio N/s_0, where s_0 is the standard deviation of the misfit between predicted and actual direction of slip along the faults. Varying the inversion parameters s, Δ, a, b, ϕ_1, and ϕ_2 for a small and reasonable amount also allows us to estimate the confidence limits for orientation of

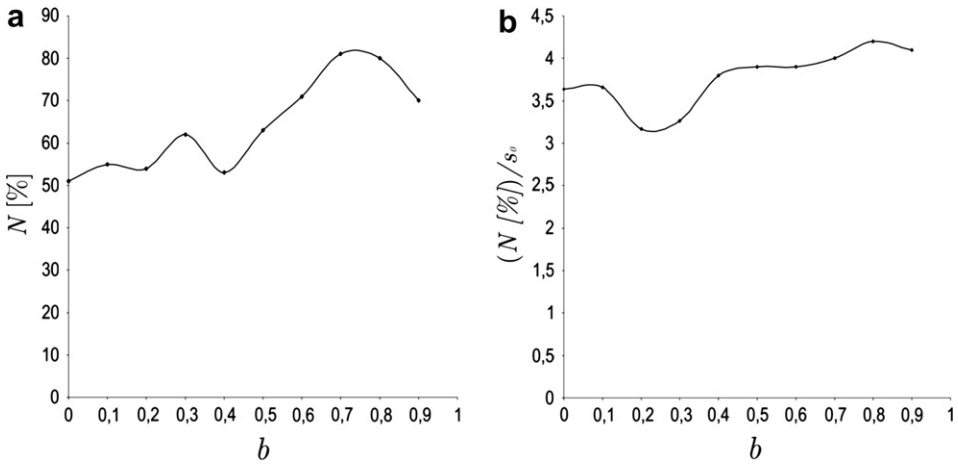

Fig. 8. (a) Dependence of the number of kinematically and mechanically compatible faults N on the constitutive parameter b. (b) Dependence of the ratio N/s_0 on the constitutive parameter b. s_0 is the standard deviation of the misfit between predicted and actual direction of slip along the faults. The best value of the parameter b leads to the inversion results with maximum number of compatible faults N and/or maximum ratio N/s_0. See text for details.

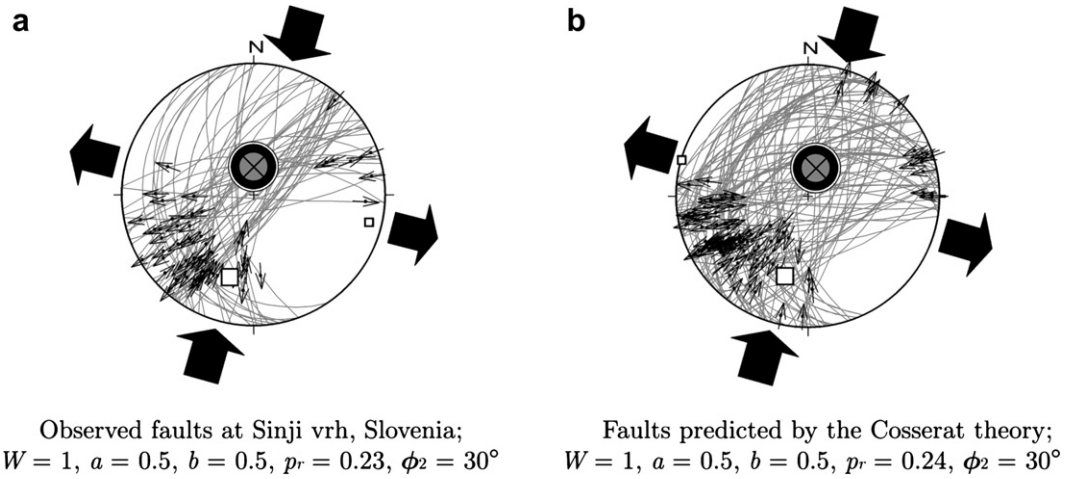

Fig. 9. Comparison of the Sinji vrh fault system with the fault system modeled using AmontonsWin. (a) The field data (see also Fig. 6b). (b) The fault system generated with AmontonsWin as predicted by the Cosserat theory for asymmetrical state of stress. See text for details.

kinematic axes, the relative magnitude of principal strains and stresses, and the magnitude and direction of the relative microrotation. The results are reliable when they are numerically stable and are in agreement with other geological data.

The second reference point on the best values for constitutive parameters a and b are the results of forward modeling with the AmontonsWin computer program. There is a strong relationship between the geometry of fault systems and asymmetry of the stress tensor (see, for example, Figs. 5e, 7 and 9). For correct values of parameters a, b and ϕ_2 (angle of friction), the modeled fault system geometry will be similar to that observed in the field. Of course, this approach only works for neoformed faults, as the geometry of reactivated fault systems is controlled by orientation of the pre-existing planes of weakness in the rock and can therefore considerably differ from that predicted by the Cosserat theory.

The reliability of the inversion results and the values of the constitutive parameters can also be verified using the Multiple-slip kinematic method (Žalohar and Vrabec, 2008), which can be extended to the Cosserat continuum (Žalohar, 2008). The Multiple-slip method allows for independent calculation of the orientation and amount of the relative microrotation. The exact description of the Cosserat extension of the Multiple-slip method is complicated, however, and would considerably exceed the scope of the present article.

11. Conclusions

1. The relative microrotation of fault-bounded blocks is directly related to the direction of slip along the faults and to the asymmetry of the active fault system, as recognized by Twiss et al. (1991, 1993) and Twiss and Unruh (1998, 2007). Symmetric fault systems can be active in the strain field characterized by zero relative microrotation. With increasing relative microrotation, the fault systems become increasingly asymmetrical. In addition, we discovered that the geometry of fault systems is defined not only by the strain, but also by the degree of asymmetry of the stress tensor.
2. The skew-symmetric component of stress only influences the shear stress on the fault planes. Increasing asymmetry of the stress tensor will consequently increase the shear stress, which can activate faults in less favorable orientations with respect to the principal axes of the macrostrain tensor, without the requirement for low residual friction values along those faults.
3. Classical determinations of principal paleostress directions become of little use when the paleostress tensor is highly asymmetrical. In such cases, the stress tensor does not have three real-valued principal directions defining orientation of planes with zero shear stress. The Cosserat model of fault reactivation suggests that the inversion of fault-slip data in fact constrains principal strain axes (kinematic axes) of the macrostrain tensor and the direction and relative magnitude of relative microrotation. The paleostress state can be reconstructed from the constitutive equation and may be used only as a tool for analyzing fault reactivation.
4. At least in some cases, there is a remarkable consistency between predictions of the Cosserat model of fault reactivation and natural fault-slip patterns and fault system geometries. We presented an example of a natural fault system which suggests (1) that faulted rocks can behave as the Cosserat continuum characterized by non-zero relative microrotations, and (2) that natural fault systems can form in asymmetric stress fields.

Acknowledgements

The authors are grateful to Robert J. Twiss for his careful review and many constructive comments. We also greatly appreciate the useful comments of an anonymous reviewer and the thorough editorial handling of Robert E. Holdsworth, who also helped to improve the language of the manuscript.

References

Angelier, J., 1989. From orientation to magnitudes in paleostress determinations using fault slip data. Journal of Structural Geology 11, 37–50.
Angelier, J., 1994. Paleostress determinations. In: Hancock, P.L. (Ed.), Continental Deformation. Pergamon Press, Tarrytown, NY, pp. 53–100.
Besdo, D., 1974. Ein Beitrag zur nichtlinearen Theorie des Cosserat-Kontinuums. Acta Mechanica 20, 105–131.
Besdo, D., 1985. Inelastic behavior of plane frictionless block-systems described as Cosserat media. Archives of Mechanics 37, 603–619.
Dai, C., Műhlhaus, H., Meek, J., Duncan Fama, M., 1996. Modeling of blocky rock masses using the Cosserat method. International Journal of Rock Mechanics and Mining Science & Geomechanics Abstracts 33, 425–432.
Dartevelle, S., 2003. Numerical and granulometric approaches to geophysical granular flows, Ph.D. thesis, Michigan Technological University.
de Borst, R., 1991. Simulation of strain localization: a reappraisal of the Cosserat continuum. Engineering Computations 8, 317–332.
de Borst, R., 1993. A generalization of J2-flow theory for polar continua. Computer Methods in Applied Mechanics and Engineering 103, 347–362.
Etse, G., Nieto, M., 2004. Cosserat continua-based micro plane modeling. Theory and numerical analysis. Latin American Applied Research 34, 229–240.

Figueiredo, R.P., Vargas, E.A., Moraes, A., 2004. Analysis of bookshelf mechanisms using the mechanics of Cosserat generalized continua. Journal of Structural Geology 26, 1931–1943.
Fleischman, K.H., Nemcok, M., 1991. Paleostress inversion of fault/slip data using the shear stress solution of Means (1989). Tectonophysics 196, 195–202.
Forest, S., 2000. Cosserat media. In: Buschow, K.H.J., Cahn, R.W., Flemings, M.C., Ilschner, B., Kramer, E.J., Mahajan, S. (Eds.), Encyclopedia of Materials: Science and Technology. Elsevier Science, Amsterdam, pp. 1715–1718.
Forest, S., Pradel, F., Sab, K., 2001. Asymptotic analysis of heterogeneous Cosserat media. International Journal of Solids and Structures 38, 4585–4608.
Forest, S., Sievert, R., 2003. Elastoviscoplastic constitutive frameworks for generalized continua. Acta Mechanica 160, 71–111.
Fry, N., 2001. Stress space: striated faults, deformation twins, and their constraints on paleostress. Journal of Structural Geology 23, 1–9.
Germain, P., Nguyen, Q.S., Suquet, P., 1983. Continuum thermodynamics. Journal of Applied Mechanics 50, 1010–1020.
Gregorič, A., 2005. Analysis of the paleostress evolution in the Dinaric thrust system in Western Slovenia (the Nova Gorica region). Unpublished Diploma, University of Ljubljana.
Hansen, E., Willam, K., Carol, I., 2001. A two-surface anisotropic damage/plasticity model for plain concrete. In: de Borst, R. (Ed.), Fracture Mechanics of Concrete Materials. Proceedings of Framos-4 Conference Paris, May 28-32, 2001. A.A. Balkema, Rotterdam, pp. 549–556.
Iordache, M.-M., Willam, K., 1998. Localized failure analysis in elastoplastic Cosserat continua. Computer Methods in Applied Mechanics and Engineering 151, 559–586.
Jaeger, J.C., Cook, N.G.W., 1969. Fundamentals of Rock Mechanics. Methuen, London.
Janež, J., Čar, J., Habič, P., Podobnik, R., 1997. Hydrological Heritage of the Central Karst. Geologija d.o.o., Idrija.
Lemaitre, J., Chaboche, J.-L., 1994. Mechanics of Solid Materials. Cambridge University Press, New York.
Lippmann, H., 1969. Eine Cosserat – Theorie des Plastischen Fliens. Acta Mechanica 8, 255–284.
Lubliner, J., 1990. Plasticity Theory. Macmillan Publishing Company, New York.
Manzari, M.T., 2004. Application of micropolar plasticity to post failure analysis in geomechanics. International Journal for Numerical and Analytical Methods in Geomechanics 28, 1011–1032.
Mohan, L.S., Nott, P.R., Rao, K.K., 1999. A frictional Cosserat model for the flow of granular materials through a vertical channel. Acta Mechanica 138, 75–96.
Mühlhaus, H.-B., Vardoulakis, J., 1987. The thickness of shear bands in granular materials. Géotechnique 37, 271–283.
Nemcok, M., Kovác, D., Lisle, R.J., 1999. A stress inversion procedure for polyphase calcite twin and fault/slip data sets. Journal of Structural Geology 21, 597–611.
Nemcok, M., Lisle, R.J., 1995. A stress inversion procedure for polyphase fault/slip data sets. Journal of Structural Geology 17, 1445–1453.
Onck, P.R., 2002. Cosserat modeling of cellular solids. C.R. Mechanique 330, 717–722.
Ranalli, G., 2000. Rheology of crust and its role in tectonic reactivation. Journal of Geodynamics 30, 3–15.
Ranalli, G., Yin, Z.-M., 1990. Critical stress difference and orientation of faults in rocks with strength anisotropies: the two-dimensional case. Journal of Structural Geology 12, 1067–1071.
Reches, Z., 1978. Analysis of faulting in three-dimensional strain field. Tectonophysics 47, 109–129.
Reches, Z., 1983. Faulting of rocks in three-dimensional strain fields II. Theoretical analysis. Tectonophysics 95, 133–156.
Reches, Z., Baer, G., Hatzor, Y., 1992. Constraints on the strength of the upper crust from stress inversion of fault slip data. Journal of Geophysical Research 97, 12. 481–12.493.
Salari, M.R., Saeb, S., Willam, K., Patchet, S.J., Carrasco, R.C., 2004. A coupled elastoplastic damage model for geomaterials. Computer Methods in Applied Mechanics and Engineering 193, 2625–2643.
Sawczuk, A., 1967. On yielding of Cosserat continua. Archives of Mechanics 19, 3–19.
Schellart, W.P., 2000. Shear test results for cohesion and friction coefficients for different granular materials: scaling implications for their usage in analogue modeling. Tectonophysics 324, 1–16.
Toupin, R.A., 1962. Elastic materials with couple stresses. Archive for Rational Mechanics and Analysis 11, 385–414.
Toupin, R.A., 1964. Theories of elasticity with couple-stresses. Archive for Rational Mechanics and Analysis 17, 85–112.
Twiss, R.J., Protzman, G.M., Hurst, S.D., 1991. Theory of slickenline patterns based on the velocity gradient tensor and microrotation. Tectonophysics 186, 215–239.
Twiss, R.J., Souter, B.J., Unruh, J.R., 1993. The effect of block rotations on the global seismic moment tensor and patterns of seismic P and T axes. Journal of Geophysical Research 98, 645–674.
Twiss, R.J., Unruh, J.R., 1998. Analysis of fault slip inversions: do they constrain stress or strain rate? Journal of Geophysical Research 103, 12.205–12.222.
Twiss, R.J., Unruh, J.R., 2007. Structure, deformation and strength of the Loma Prieta fault, northern California, USA, as inferred from 1989–1990 Loma Prieta aftershock sequence. GSA Bulletin 119, 1079–1106.
Udias, A., 1999. Principles of Seismology. Cambridge University Press, Cambridge.
Veselič, M., Čenčur Curk, B., Šebela, S., 1998. An evaluation of structural analysis of discontinuities in carbonate rock. Geological Journal 33, 205–221.
Vrabec, M., Fodor, L., 2006. Late Cenozoic tectonics of Slovenia: structural styles at the north eastern corner of the adriatic microplate. In: Pinter, N. (Ed.), The Adria Microplate: GPS Geodesy, Tectonics and Hazards. NATO Science Series IV, vol. 61. Earth and Environmental Sciences, pp. 151–168.
Willam, J.K., 2002. In: Encyclopedia of Physical Science and TechnologyConstitutive models for engineering materials, third ed, vol. 3. Academic Press, New York, pp. 603–633.
Willam, K.J., Iordache, M.-M., 2001. On the lack of symmetry in materials. In: Wall, W.A., Bletzinger, K.U., Schweizerhof, K. (Eds.), International Center for Numerical Methods in Engineering. Proceedings of International Conference on Trends in Computational Structural Mechanics, Schloss Hofen, Austria, May 20–23, 2001. CIMNE-UPC, Barcelona, pp. 233–242.
Yin, Z.-M., Ranalli, G., 1992. Critical stress difference, fault orientation and slip direction in anisotropic rocks under non-Andersonian stress systems. Journal of Structural Geology 14, 237–244.
Yin, Z.-M., Ranalli, G., 1995. Estimation of the frictional strength of faults from inversion of fault-slip data: a new method. Journal of Structural Geology 17, 1327–1335.
Žalohar, J., Vrabec, M., 2007. Paleostress analysis of heterogeneous fault-slip data: the Gauss method. Journal of Structural Geology 29, 1798–1810.
Žalohar, J., 2008. Cosserat strain and stress analysis of heterogeneous fault systems with the Gauss method. Ph.D. thesis, University of Ljubljana.
Žalohar, J., Vrabec, M., 2008. Combined kinematic and paleostress analysis of fault-slip data: the multiple-slip method. Journal of Structural Geology 30, 1603–1613.